L. Rodriguez-Suñé, M. Scalora, A. S. Johnson, C. Cojocaru, N. Akozbek, Z. J. Coppens, D. Perez-Salinas, S. Wall, and J. Trull "Second harmonic generation from an ITO nanolayer: experiment versus theory", Proc. SPIE 11345, Nanophotonics VIII, 113451R (1 April 2020); https://doi.org/10.1117/12.2555393

Second harmonic generation from an ITO nanolayer: experiment versus theory

L. Rodríguez-Suné*[a], M. Scalora[b], A. S. Johnson[c], C. Cojocaru[a], N. Akozbek[d], Z. J. Coppens[d], D. Perez-Salinas[b], S. Wall[b], J. Trull[a]

[a]Department of Physics, Universitat Politècnica de Catalunya, Rambla Sant Nebridi 22, 08222 Terrassa, Spain; [b]Charles M. Bowden Research Center, CCDC AVMC, Redstone Arsenal, AL 35898-5000 USA; [c]ICFO – The Institute of Photonic Sciences, The Barcelona Institute of Science and Technology, 08860 Castelldefels, Spain; [d]AEgis Technologies Inc., 401 Jan Davis Dr., Huntsville Alabama 35806, USA

ABSTRACT

We report a comparative experimental and theoretical study of second harmonic generation from a 20nm-thick indium tin oxide nanolayer in the proximity of the epsilon-near-zero condition. We record the efficiency of the second harmonic signal both as a function of wavelength as well as of the angle of incidence around the epsilon-near-zero crossing point. We compare our experimental results with numerical simulations based on a hydrodynamical model able to capture all major physical mechanisms driving the electrodynamic behavior of conductive oxide layers, with unique aspects of the different nonlinear sources. We found a very good quantitative and qualitative agreement between experiment and theory.

Keywords: nonlinear harmonic generation, epsilon-near-zero, conductive oxide

1. INTRODUCTION

Second and third harmonic generation (SHG and THG), as the most fundamental processes in nonlinear optics, have been extensively studied in different optical materials, usually looking for high conversion efficiencies which are achieved with highly nonlinear materials, phase-matching conditions and low material absorption at the fundamental and second harmonic (SH) wavelengths. When the nonlinear material size is reduced at the nanoscale SH efficiencies drastically decrease and phase matching conditions and even absorption may no longer play a significant role. The combination of geometrical features, resonances, bound electrons, and nonlocal, surface and magnetic effects on free electrons can substantially modify the material response as well as the very nature of linear and nonlinear light-matter interactions. At the nanometer scale conventional approximations to the dynamics of light-matter interactions break down, so new strategies must be sought in order to study, understand and harness the performance of sub-wavelength nonlinear optical materials which nowadays are routinely produced and integrated in different devices and applications.

A new class of optical materials, displaying vanishingly small real part of the dielectric constant, known as epsilon-near-zero (ENZ) materials, have been recently proposed as promising platforms for the extreme enhancement of the electromagnetic field [1,2]. As a consequence, nonlinear optical phenomena are also enhanced. Although the ENZ materials are usually obtained artificially, all-natural materials that display a Lorentz-like response also exhibit a real part of the dielectric permittivity that crosses zero, in proximity of either plasma or interband transition frequencies [2]. For instance, semiconductors like GaAs, GaP and Si display ENZ conditions near 100nm, deep in the ultraviolet range. Metals like Au, Ag and Cu have ENZ crossing points in the visible range, while the zero-crossing points of conducting oxides like indium tin oxide (ITO) and cadium oxide (CdO) fall in the infrared regime. The main limitations for field enhancement in ENZ materials are thought to be related to the narrow-band nature of the crossing "point", and absorption.

Conducting oxides, as well as metals, are free electron systems. However, their linear and nonlinear optical properties are not exactly the same. Free electron densities of noble metals can be several orders of magnitude larger than the free electron densities of conducting oxides. This leads to significant differences in field penetration and the excitation of surface and volume nonlinearities, and nonlocal effects [3]. Moreover, noble metals are characterized by interband transitions, increased free carrier density and a dynamic blueshift of plasma frequency, while conducting oxides display intraband transitions and increased electron gas temperature that lead to increased effective electron mass and a dynamic redshift of

Nanophotonics VIII, edited by David L. Andrews, Angus J. Bain, Martti Kauranen, Jean-Michel Nunzi, Proc. of SPIE Vol. 11345, 113451R · © 2020 SPIE
CCC code: 0277-786X/20/$21 · doi: 10.1117/12.2555393

the plasma frequency [4]. Compared to noble metals, these effects make conducting oxides intriguing for the experimental and theoretical study of nonlinear optical interactions.

Several studies of SHG and THG from ITO have been reported, most of them based on experimental observations [5-7]. However, in all these studies no comprehensive and satisfactory theoretical model has been presented, that sheds light on the competing physical mechanisms that characterize the interaction. For instance, it is known that nonlocal effects tend to blueshift the plasmonic resonance. In contrast, absorption, which is in turn modified by nonlocal effects, can change the free electron effective mass, causing the plasma frequency to redshift [4]. Nonlocal effects and modulation of the plasma frequency are dynamic, time dependent factors that can strongly influence the propagation, and can easily combine to impress unique dynamical features on measurable quantities, such as spatial and temporal modulation of dielectric constant and refractive index. Nevertheless, most models rely either on the introduction of phenomenological or effective parameters, or on qualitative, seemingly plausible arguments that may help one glimpse the nature of the interaction.

In view of our discussion above, in this work we first present experimental measurements of SHG from a 20nm-thick ITO layer as a function of incident laser pulse wavelength in order to demonstrate and quantify the resonance-like properties that occur at the ENZ spectral position. We then go on to show the angular dependence of SHG for different input wavelengths in order to highlight the metal-like response, an aspect which is often neglected in conducting oxides and that typically yields maximum SHG at large angles. Finally, we will describe the most important aspects of the theoretical model, and compare with experimental results.

2. EXPERIMENTAL SET-UP AND RESULTS

. A schematic representation of the set-up used in our experiments is shown in Fig. 1. As nonlinear material we used a 20nm-thick ITO layer deposited on top a a glass substrate, which displayed an ENZ condition near 1260nm. We recorded the SH signal generated by the ITO sample as a function of the fundamental field wavelength, as well as a function of the angle of incidence. The spectral measurements were performed using anoptical parametric oscillator (OPA) (TOPAS, Light Conversion) pumped by 4mJ pulses from a Ti:Sapphire amplifier (Astrella, Coherent) delivering continuously-tunable pulses in a wavelength range from 1140nm to 1600nm, with energies of 0.5mJ/pulse generated at a repetition rate of 1kHz. A long-pass filter was used to remove the residual pump and other sum-frequency components coming from the OPA wire grid polarizer and a super-achromatic waveplate was employed to prepare and control the input beam polarization. The pulses were attenuated down to tens of μJ using reflective, neutral density filters. For the characterization of the input beam parameters at the plane of the sample, knife-edge and FROG measurements were carried out. Depending on the wavelength, beam waists between 4.2mm and 4.8mm at $1/e^2$ radius in intensity and pulse durations between 50fs and 102fs FWHM were measured, leading to typical power densities between 1 and 2GW/cm^2. Any possible SH signals arising from portions of the set-up placed before the ITO sample were filtered using band-pass filters. The ITO sample was mounted on a rotary support ensuring precise control of the fundamental beam incident angleAfter the sample, a lens with focal length f = 100mm was used to collimate the light, and the polarization of the generated SH was analyzed by a polarizer. Different filters were used to attenuate the fundamental beam immediately after the sample in order to avoid any possible harmonic generation arising from other surfaces of optical elements placed after the ITO sample. A prism and a sharp edge were used to separate and obscure the remaining fundamental radiation from the SH path. A photomultiplier tube was used to detect the SH signal together with a narrow-band spectral filter having 20nm band pass transmission

around the SH frequency. The entire detection system was mounted on a rotating rigid platform in order to measure transmission and reflection of the generated SH signals.

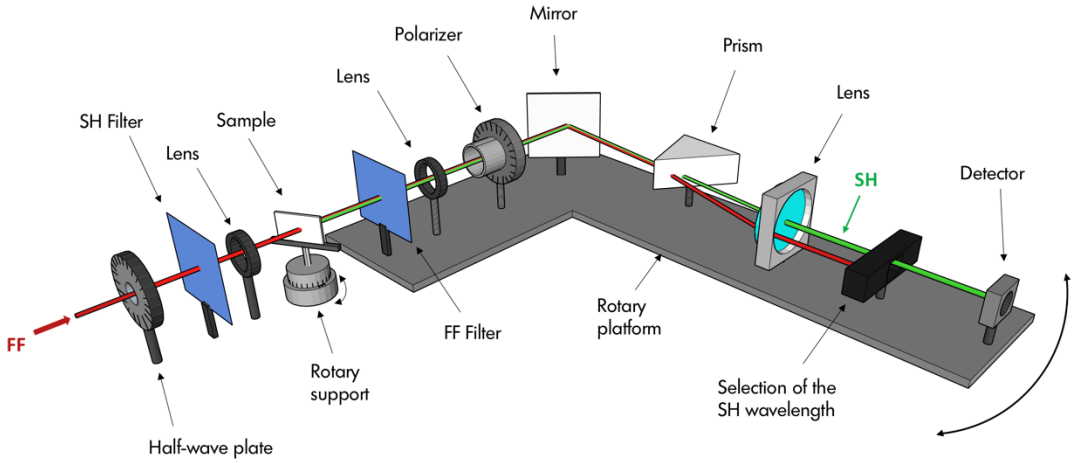

Figure 1: Setup for measuring SH signal. The whole platform after the sample is mounted on a rotating arm to be used for transmission or reflection measurements. FF filters correspond to low pass filters (Schott KG3 and BG40) which are placed after the sample and are used to eliminate the fundamental radiation.

First of all, we measured the SH efficiency as a function of the fundamental wavelength around the ENZ condition, for a fixed incident angle of 60º. We have collected these results in Fig. 2(a), where it can be seen the spectral response of the SH generated both in transmission (dashed red curve, open squares) and in reflection (dashed blue curve, open circles). It can be clearly observed that the SHG conversion efficiency is enhanced near the ENZ condition, appearing near 1240nm. It can also be observed that the locations of reflected and transmitted maxima do not coincide, most likely because transmission hinges more on propagation through the bulk material, while the reflected component partially benefits from conditions at the surface(s). This relative shift between transmitted and reflected maxima was previously unknown. Another experiment consisted in measuring the generated SH in transmission as a function of the angle of incidence for three different input carrier wavelengths: above (1300nm), at (1240nm) and below (1200nm) the ENZ condition. This is shown in Fig. 2(b).

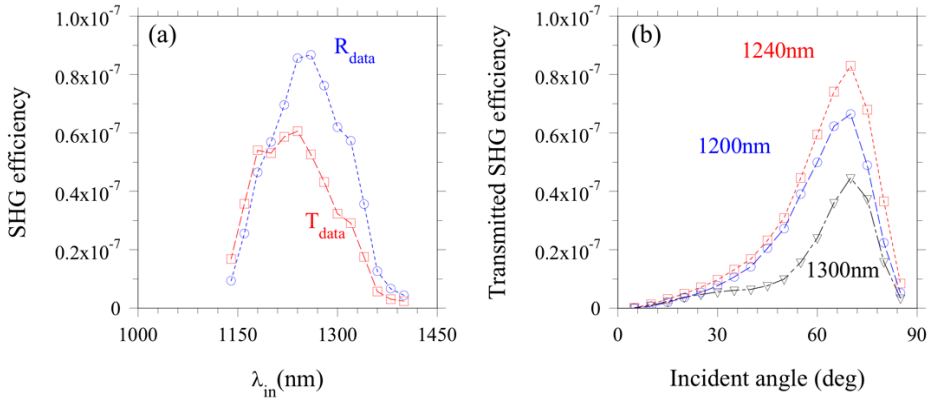

Figure 2: (a) Experimental data of reflected (dashed blue curve, open circle markers) and transmitted (dashed red curve, open squares markers) SHG efficiency from a 20nm-thick ITO layer vs. input carrier wavelength. (b) Angular dependence of transmitted SHG vs. incident angle at the indicated carrier wavelengths.

3. THEORETICAL APPROACH

In order to understand and compare the experimental results, we have carried out numerical simulations based on a theoretical approach that embraces full scale time-domain coupling of matter to the macroscopic Maxwell's equations. Usually, models where just the magnitude of the nonlinear index change is sought using a unidirectional beam propagation method with an effective nonlinearity of unspecified origin are used. On the contrary, our strategy is based on formulating a microscopic, hydrodynamic approach that accounts for competing surface, magnetic, and bulk nonlinearities arising from both free and bound charges, preserving linear and nonlinear dispersion, nonlocal effects due to pressure and viscosity, changes in the effective mass of free electrons triggered by absorption, and even pump depletion, should local field intensities be so large to require it.

The theoretical description of the macroscopic electrodynamics of conducting oxides we use in our model is not only given by the typical used Drude model, but also takes into account bound electron resonances having a Lorentzian response peaked somewhere in the UV range. So, at the end we use a combined Drude-Lorentz model given by Eq. 1:

$$\varepsilon_{\mathrm{ITO}}(\omega) = 1 - \frac{\omega_{\mathrm{p,b}}^2}{\omega^2 - \omega_{0,\mathrm{b}}^2 + \mathrm{i}\gamma_{\mathrm{b}}\omega} - \frac{\omega_{\mathrm{p,f}}^2}{\omega^2 + \mathrm{i}\gamma_{\mathrm{f}}\omega} \tag{1}$$

where $\omega_{\mathrm{p,f}} = \frac{4\pi n_{0,\mathrm{f}} e^2}{m_{\mathrm{f}}^*}$ is the free electron plasma frequency, $n_{0,\mathrm{f}}$ is the free electron density, e is the electronic charge, γ_{f} is the free electron damping coefficient, m_{f}^* is the temperature-dependent effective free electron mass, $\omega_{\mathrm{p,b}}$ is the bound electron plasma frequency, $\omega_{0,\mathrm{b}}$ is the resonant frequency, and γ_{b} is the bound electron damping coefficient.

This description of the dielectric function of ITO adds a pivotal, dynamical dimension that is usually disregarded: the Lorentzian response triggers an intrinsic, dispersive, resonant nonlinearity that may compete with the nonlinearity introduced by heating the free carriers, depending on tuning and incident pump intensity. However, this description of ENZ materials is limited by one aspect: it neglects to include the impact of nonlocal effects.

For this reason, we proceed now to write the coupled material equations of motion that describe two separate polarization components produced by free and bound electrons, without explicitly introducing the dielectric constant, or making any other assumption. By fitting the retrieved, local dielectric function, damping coefficients, effective masses, and densities can be determined and be inserted in the dynamical equations of motion. Both equations simultaneously contain lowest order contributions of bulk, surface and magnetic nonlinearities, which we now adapt from our previous work on nonlinear optics of metals [8-12] and semiconductors [13,14], by modifying them to include the dynamics that ensues with a temperature and thus time-dependent plasma frequency:

$$\ddot{\mathbf{P}}_{\mathrm{f}} + \tilde{\gamma}_{\mathrm{f}}\dot{\mathbf{P}}_{\mathrm{f}} = \frac{n_{0,\mathrm{f}} e^2 \lambda_0^2}{m_{\mathrm{f}}^*(T_{\mathrm{e}}) c^2}\mathbf{E} - \frac{e\lambda_0}{m_{\mathrm{f}}^*(T_{\mathrm{e}}) c^2}\mathbf{E}(\nabla\cdot\mathbf{P}_{\mathrm{f}}) + \frac{e\lambda_0}{m_{\mathrm{f}}^*(T_{\mathrm{e}}) c^2}\dot{\mathbf{P}}_{\mathrm{f}}\times\mathbf{H} +$$
$$+ \frac{3E_{\mathrm{F}}}{5m_{\mathrm{f}}^*(T_{\mathrm{e}}) c^2}\left(\nabla(\nabla\cdot\mathbf{P}_{\mathrm{f}}) + \frac{1}{2}\nabla^2\mathbf{P}_{\mathrm{f}}\right) - \frac{1}{n_{0,\mathrm{f}} e c}\left[(\nabla\cdot\dot{\mathbf{P}}_{\mathrm{f}})\dot{\mathbf{P}}_{\mathrm{f}} + (\dot{\mathbf{P}}_{\mathrm{f}}\cdot\nabla)\dot{\mathbf{P}}_{\mathrm{f}}\right] \tag{2}$$

$$\ddot{\mathbf{P}}_{\mathrm{b}} + \tilde{\gamma}_{\mathrm{b}}\dot{\mathbf{P}}_{\mathrm{b}} + \tilde{\omega}_{0,\mathrm{b}}^2\mathbf{P}_{\mathrm{b}} + \mathbf{P}_{\mathrm{b,NL}} = \frac{n_{0,\mathrm{b}} e^2 \lambda_0^2}{m_{\mathrm{b}}^* c^2}\mathbf{E} + \frac{e\lambda_0}{m_{\mathrm{b}}^* c^2}(\mathbf{P}_{\mathrm{b}}\cdot\nabla)\mathbf{E} + \frac{e\lambda_0}{m_{\mathrm{b}}^* c^2}\dot{\mathbf{P}}_{\mathrm{b}}\times\mathbf{H} \tag{3}$$

Eqs. 2 and 3 describe the dynamics of free and bound electrons, respectively; T_{e} is the free electron temperature; $\mathbf{P}_{\mathrm{b,NL}} = \alpha\mathbf{P}_{\mathrm{b}}\mathbf{P}_{\mathrm{b}} - \beta(\mathbf{P}_{\mathrm{b}}\cdot\mathbf{P}_{\mathrm{b}})\mathbf{P}_{\mathrm{b}} + \cdots$ is the bound electron's nonlinear polarization; m_b^* is the bound electron mass; $n_{0,\mathrm{b}}$ is the bound electron density, $\tilde{\gamma}_{\mathrm{f,b}} = \gamma_{\mathrm{f,b}}\lambda_0/c$, $\tilde{\omega}_{\mathrm{f,b}}^2 = \omega_{\mathrm{f,b}}^2\lambda_0^2/c^2$. Time and space have been scaled such that temporal and spatial derivatives are carried out with respect to the following dimensionless coordinates: $\zeta = y/\lambda_0$, $\xi = z/\lambda_0$, and $\tau = ct/\lambda_0$. $\lambda_0 = 1\mu\mathrm{m}$ is a convenient reference wavelength.

The coefficients α and β are also scaled accordingly, are to be interpreted as tensors, and carry information about crystal symmetry. The combination of Eqs. 2 and 3 thus preserves both linear and nonlinear dispersion. The free electron component in ITO is similar to that of noble metals, except for the fact that m_{f}^* is now a function of temperature. In summary, the first and second terms on the right hand side of Eq. 2 are Coulomb terms, followed by the magnetic Lorentz term, nonlocal terms (pressure and viscosity) and ending with convective terms. On the right hand side of Eq. 4 we have the bound electron plasma frequency, followed by surface and magnetic Lorentz contributions.

When the electron temperature is only a few thousand degrees Kelvin, the description of hot carriers can be approximated by:

$$m_f^*(T_e) \approx m_0^* + K_B T_e = m_0^* + K_B \Lambda \int \mathbf{J} \cdot \mathbf{E}\, dt \tag{4}$$

where K_B is Boltzman's constant; Λ is a constant of proportionality; m_0^* is the electron's rest mass for no applied field; $\Lambda \int \mathbf{J}\cdot\mathbf{E}\, dt$ represents absorption; and $\mathbf{J}=\dot{\mathbf{P}}_f$ is the current density derived from Eq. 2, which contains intrinsic modifications imparted to the dielectric response by nonlocal effects and hot electron contributions. However, for our present purpose and for convenience in what follows we will assume the simplified form $\mathbf{J}=\sigma_0\mathbf{E}$, where σ_0 is a constant to be determined. Using the temperature dependent expression for the effective mass Eq. 4, the leading term on the right hand side of Eq. 2 may be written as:

$$\frac{n_{0,f} e^2 \lambda_0^2}{m_f^*(T_e) c^2}\mathbf{E} \approx \frac{n_{0,f} e^2 \lambda_0^2}{m_0^* c^2}\mathbf{E} - \tilde{\Lambda}(\mathbf{E}\cdot\mathbf{E})\mathbf{E} + \tilde{\Lambda}^2(\mathbf{E}\cdot\mathbf{E})^2\mathbf{E} \tag{5}$$

where for simplicity we have introduced a parameter $\tilde{\Lambda}$ proportional to the product of $\frac{\Lambda\sigma_0}{m_0^*}$ and the temporal duration of the pulse. The effective mass appears in all but one term on the right hand side of Eq. 2. However, additional nonlinear contributions beyond Eq. 5 to the rest of the terms of Eq. 2 are of higher order, and for our present purposes may be neglected.

The coefficient $\tilde{\Lambda}$ thus determines the spatio-temporal dynamics of the redshift impressed upon the plasma frequency. While this discussion leaves Eq. 3 unaltered, the first term on the right hand side of Eq. 2 takes the form of Eq. 5, and includes cubic and quintic nonlinearities. Finally, using the solutions of Eqs. 2, 3 and 5 the total polarization is written as the vector sum of free and bound electron contributions, $\mathbf{P}_{total}=\mathbf{P}_f+\mathbf{P}_b$, and is inserted into Maxwell's equations.

4. EXPERIMENTAL VERSUS THEORETICAL RESULTS

In Fig. 3(a) we show both experimental data (same as in Fig.2a), as well as the simulation predictions of the transmitted (dashed red curve, open squares) and reflected (dashed blue curve, open circles) SHG efficiency as a function of the input carrier wavelength, at the fixed incident angle of 60ºThe solid curves labeled T_{sim} (red) and R_{sim} (blue) are the corresponding SH spectra calculated by integrating the material Eqs. 2, 3 and 5 together with the Maxwell's equations, using pulses of approximately 100 fs that are plane in the transverse direction to remove diffraction effects. Conversion efficiencies may be defined as the ratio of either peak intensities or pulse energies interchangeably, with identical results. In Fig. 3(b) the experimentally-retrieved, local complex dielectric constant of our ITO sample is plotted. The real part of the dielectric function crosses zero near 1260nm. The data is fitted using the Drude-Lorentz model described by Eq. 1. The curve is strongly indicative of the fact that material dispersion is Drude-like above 450nm and Lorentz-like at smaller wavelengths. In Fig. 3(c) we have plotted transmitted SHG efficiencies in order to illustrate the contrasting actions of nonlocal and hot electron contributions.

According to the structure of Eq. 2, when incident power density increases, the plasma frequency and thus the ENZ condition is redshifted, affecting SHG. The effective electron mass determines the nonlinear gain arising from Coulomb and magnetic Lorentz terms, while the density affects the nonlinear gain due to convection. By the same token, m_0^* and $n_{0,f}$ determine the Fermi energy and thus the degree of blueshift the ENZ peak experiences. The calculations are performed using a power density of 1GW/cm^2. The effective free electron mass and density are chosen as $m_0^*=0.033m_e$ and $n_{0,f}\sim 10^{20}$cm^{-3}, which combine a Fermi energy that imparts a blueshift of nearly 50nm to the SHG-peak spectral position. The magnitude of $\tilde{\Lambda}$ is chosen so that its effect is to redshift the SHG spectra by approximately 15nm, for a net blueshift of ~35nm. The integration of the equations of motion is carried out using a spectral method to propagate the fields, and a predictor-corrector algorithm to integrate the material equations.

The reproduction of experimental conditions and results depends on a balance between all these aforementioned factors, which are pivotal but whose magnitudes cannot be known precisely. Nevertheless, the agreement we find between experiments and simulations is quite extraordinary. As can be seen in Fig. 3(a), both the location of the transmitted and

reflected SH peaks and the ratio between transmitted and reflected maxima are almost the same for experimental results and simulations.

In Fig. 3(d) we have plotted the angular dependence of transmitted SHG efficiency (dashed red curve, empty squares) at 1240nm input carrier wavelength previously shown in Fig. 2(b). At the same time, the predicted (solid green curve, full triangles) transmitted SHG efficiency at that same input wavelength is represented. Once again we find very good qualitative and quantitative agreement between our experimental observations and the predicted curves. The SH efficiency peak, which occurs near 70º, and the shape of the curve depend on the magnitude of the nonlocal coefficient, and to the extent it is counteracted by pump absorption and electron cloud heating.

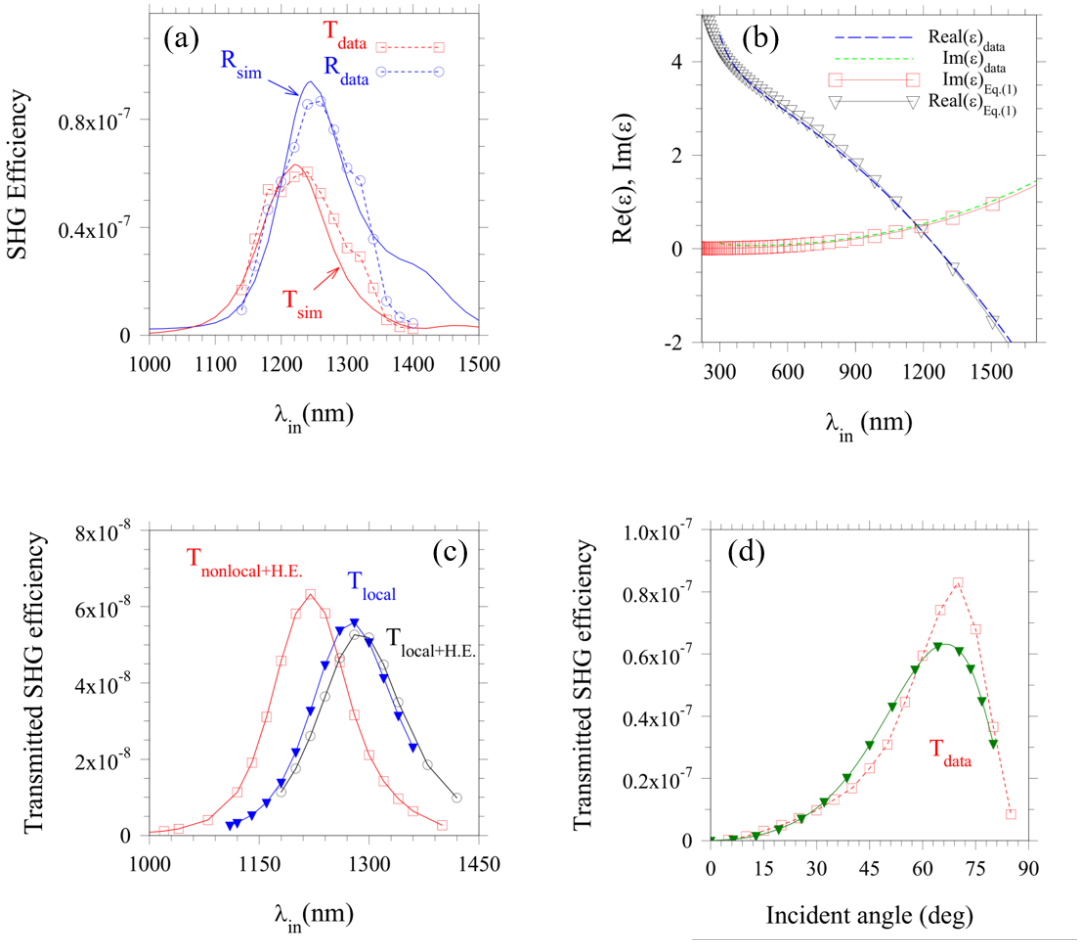

Figure 3: (a) Experimental measurement of reflected (dashed blue curve, open circle markers) and transmitted (dashed red curve, open square markers) SHG efficiency from 20nm-thick ITO layer vs. input carrier wavelength, as in Fig. 2(a). The solid curves labeled T_{sim} (red) and R_{sim} (blue) are the corresponding theoretical predictions, as indicated by the respective arrows. (b) Data corresponding to real and imaginary parts of the dielectric constant (long blue dashes, and short green dashes, respectively) retrieved from ellipsometric analysis, fitted using the Drude-Lorentz oscillators in Eq. 1, as indicated in the legend. The real part of the dielectric constant crosses zero near 1260nm. (c) Transmitted SHG efficiency vs. input carrier wavelength. The subscript "H.E." refers to hot electrons. The blue curve (solid triangle markers) labeled T_{local} is obtained by setting $\frac{3E_F}{5m_0^* c^2}=0$ and $\tilde{\Lambda}=0$, i.e. without nonlocal effects or hot electrons. The black curve (open circle markers) is redshifted by approximately 15nm with respect to the local curve, and is calculated with $\frac{3E_F}{5m_0^* c^2}=0$ and $\tilde{\Lambda}=10^{-9}$. The red curve (open squares) labeled $T_{nonlocal+H.E.}$ is blueshifted by approximately 35nm with respect to the local curve, and includes nonlocal and hot electron effects, $\frac{3E_F}{5m_0^* c^2}=3.48\cdot10^{-5}$ and $\tilde{\Lambda}=10^{-9}$. (d) Measured (dashed red curve, empty squares, T_{data} from Fig. 2(b)) and predicted (solid green curve, full triangles) transmitted SHG efficiency from 20nm-thick ITO as a function of the angle of incidence for 1240nm.

5. CONCLUSIONS

We have presented experimental results and theoretical predictions on the spectral and angular dependence of the SHG efficiency generated by a 20nm-thick ITO layer, close to the ENZ point The results suggest that transmitted and reflected SHG spectra display maxima that are shifted by approximately 20nm with respect to each other, which has not been reported before. We have also outlined a new theoretical approach based on a microscopic, hydrodynamic model that takes into account nonlocal effects, a time-dependent plasma frequency, surface and magnetic effects, convection and bound electron contributions that collectively give rise to surface and bulk generated harmonic signals in conducting oxides. We have implemented an accurate propagation model that takes into account these physical factors in a realistic environment, without the manifestation of artificial, misleading singularities. To the best of our knowledge we are not aware of any other theoretical approach that is as comprehensive as outlined in this work, and that yields qualitatively and quantitatively accurate results in a context where the only free parameters are effectively free electron mass and density. In this regard, we expect our theoretical model to be applicable to other nonlinear interactions in ENZ materials and provide deeper understanding of the phenomenon.

REFERENCES

[1] M. Z. Alam, I. D. Leon, and R. W. Boyd, "Large optical nonlinearity of indium tin oxide in its epsilon-near-zero region," Science **352**, 795 (2016).

[2] M. A. Vincenti, D. de Ceglia, A. Ciattoni, and M. Scalora, "Singularity-diven second- and third-harmonic generation at ε-near-zero crossing points," Phys. Rev. A **84**, 063826 (2011).

[3] D. de Ceglia, M. A. Vincenti, N. Akozbek, M. J. Bloemer, and M. Scalora, "Nested plasmonic resonances: Extraordinary enhancement of linear and nonlinear interactions," Opt. Express **25**, 3980 (2017).

[4] Y. Yang, K. Kelley, E. Sachet, S. Campione, T. S. Luk, J. P. Maria, M. B. Sinclair, and I. Brener, "Femtosecond optical polarization switching using a cadium oxide-based perfect absorber," Nature Photonics **11**, 390-395 (2017).

[5] T. S. Luk, D. de Ceglia, S. Liu, G. A. Keeler, R. P. Prasankumar, M. A. Vincenti, M. Scalora, M. B. Sinclair, and S. Campione, "Enhanced third harmonic generation from epsilon-near-zero modes of ultrathin films," Appl. Phys. Lett. **106**, 151103 (2015).

[6] A. Capretti, Y. Wang, N. Engheta, and L. D. Negro, "Enhanced third-harmonic generation in si-compatible epsilon-near-zero indium tin oxide nanolayers," Opt. Lett. **40**, 1500-1503 (2015).

[7] A. Capretti, Y. Wang, N. Engheta, and L. D. Negro, "Comparative study of second-harmonic generation from epsilon-near-zero indium tin oxide and titanium nitride nanolayers excited in the near-infrared range," ACS Photonics **2**, 1584-1591 (2015).

[8] D. de Ceglia, M. Scalora, M. A. Vincenti, S. Campione, K. Kelley, E. L. Runnerstrom, J. P. Maria, G. A. Keeler, and T. S. Luk, "Viscoelastic optical nonlocality of low-loss epsilon-near-zero nanofilms," Scientific Rep. **8**, 9335 (2018).

[9] M. Scalora, M. Vincenti, D. de Ceglia, N. Akozbek, M. Bloemer, C. D. Angelis, J. Haus, R. Vilaseca, J. Trull, and C. Cojocaru, "Harmonic generation from metal-oxide and metal-metal boundaries," Phys. Rev. A **98**, 023837 (2018).

[10] M. Scalora, M. A. Vincenti, D. de Ceglia, V. Roppo, M. Centini, N. Akozbek, and M. J. Bloemer, "Second- and third-harmonic generation in metal-based structures," Phys. Rev. A **82**, 043828 (2010).

[11] M. Scalora, M. Vincenti, D. de Ceglia, N. Akozbek, V. Roppo, M. Bloemer, and J. W. Haus, "Dynamical model of harmonic generation in centrosymmetric semiconductors at visible and uv wavelengths," Phys. Rev. A **85**, 053809 (2012).

[12] M. Scalora, M. A. Vincenti, D. de Ceglia, C. M. Cojocaru, M. Grande, and J. W. Haus, "Nonlinear duffing oscillator model for third harmonic generation," J. Opt. Soc. Am. B **32**, 2129 (2015).

[13] L. Rodriguez-Sune, J. Trull, M. Scalora, R. Vilaseca, and C. Cojocaru, "Harmonic generation in the opaque region of gaas: the role of the surface and magnetic nonlinearities," Opt. Express **27**, 26120–26130 (2019).

[14] M. Scalora, J. Trull, C. Cojocaru, M. Vincenti, L. Carletti, D. de Ceglia, N. Akozbek, and C. D. Angelis, "Resonant, broadband and highly efficient optical frequency conversion in semiconductor nanowire gratings at visible and uv wavelengths," J. Opt. Soc. Am B **36**, 2346–2351 (2019).